

# Vortex Lattice Method Coupled with Advanced One-Dimensional Structural Models

(Received: Jan. 24, 2011. Revised: July 28, 2011. Accepted: Aug. 1, 2011)

ALBERTO VARELLO<sup>1,2</sup>  
ERASMO CARRERA<sup>1</sup>  
LUCIANO DEMASI<sup>3</sup>

## Abstract

This work couples a Vortex Lattice Method, VLM, to a refined one-dimensional structural model based on Carrera Unified Formulation, CUF. Airfoil in-plane deformation and warping are introduced by enriching the displacement field over the cross-section of the wing. Linear to fourth-order expansions are adopted and classical beam theories (Euler-Bernoulli and Timoshenko) are obtained as particular cases. The VLM aerodynamic theory is coupled via an appropriate adaptation of the Infinite Plate Spline method to the structural finite element model. A number of wing configurations (by varying aspect ratio, airfoil geometry, dihedral, and sweep angle) and load cases are analyzed to assess both the calculation of aerodynamic loadings and the influence of in-plane airfoil deformation to the static response of the wing. Comparison with shell results of commercial software such as MSC Nastran, which is taken as reference solution, is carried out and discussed. The importance of higher-order models for an accurate evaluation of local and global response of aircraft wings is shown.

## 1. Introduction

The accurate structural response of deformable lifting bodies (LBs) when subjected to steady and unsteady aerodynamic loadings consists in a typical challenging issue for the aeroelastic design of aerospace vehicles. This topic mostly involves the three following points: accurate evaluation of aerodynamic loadings for a given LB geometry; description of deformation of LBs when subjected to known forces; interaction between aerodynamics and structural behavior. A number of significant contributions have been given on these matters. First [31], [4], and then more recent books such as [37] and [60] describe in detail known methods and techniques used to define the aeroelastic phenomena of LBs. The accessibility to commercial software such as MSC Nastran and ZAERO allows the effectiveness and robustness of some available aeroelastic models to be demonstrated.

In order to develop tools able to work at any regime and with any LB geometry (including rotating blades), literature from the last decades has been widely influenced by research devoted to building reliable methods to couple computational fluid dynamics, CFD (at any regime, viscous and inviscid), with the finite element method, FEM, for the structural modeling, see Farhat [30]. Many review articles about fluid-structure interaction have been written and those by Dowell and Hall [26], Guruswamy [33], Kamakoti and Shyy [39], and Henshaw et al. [36] are herein mentioned. Recent advances in describing fluid-structure interaction for flapping wing aeroelasticity can be found in Shyy et al. [52].

Among the various issues involved in aeroelastic design, the present work focuses on the development of advanced one-dimensional computational structural models for aircraft wings. Compared to plates and shells, 1D models require less computational effort. This requisite is of particular interest for the analysis of those aeroelastic problems in which a strong non-linear coupling must be described. The one-dimensional models used in early studies of wing-like structures were based on classical beam theories, such as those founded on

---

<sup>1</sup> Department of Aerospace Engineering, Politecnico di Torino, Torino, Italy

<sup>2</sup> Institut Jean Le Rond d'Alembert, UMR 7190, CNRS, Univ Paris 6, Paris, France

<sup>3</sup> San Diego State University, San Diego, CA 92182, USA

Euler-Bernoulli's [29] and Timoskenko's [56] assumptions. Unfortunately, airfoil in-plane deformation and warping is not taken into account by these models. As a consequence, classical beam models do not capture with sufficient accuracy the displacement field necessary for an efficient aeroelastic CFD-FEM coupling. Therefore it is not surprising that well known aerodynamic techniques such as the Vortex Lattice Method (VLM) and the Doublet Lattice Method (DLM) normally refer to wings modeled by plates/shells. However, advanced 1D structural models would permit a useful and not less effective interaction with CFD as well as with VLM and DLM.

In the past, many attempts have been proposed to overcome the limitations of classical beam theories and to permit the application of 1D models to any wing geometry. In addition to many examples described in well-known books on the theory of elasticity (see [46]), recently developed beam models have been obtained via different approaches:

- introduction of shear correction factors;
- use of warping functions;
- variational asymptotic solutions (VABS);
- generalized beam theories (GBT);
- higher-order beam models.

A review was carried out by Kapania and Raciti [40, 41], whereas a recent detailed review of such models can be found in Carrera et al.[17]. A considerable amount of work has been done in trying to improve the global response of classical beam theories using appropriate shear correction factors, as in the books by Timoshenko [56] and Sokolnikoff [55]. Among the many available articles, the works by Cowper [21], Murthy [43], and Mechab et al.[45] are of particular interest. El Fatmi [27, 28] improved on the displacement field over the beam cross-section by introducing a warping function to refine the description of normal and shear stress of the beam.

An asymptotic type expansion in conjunction with variational methods has been proposed by Berdichevsky et al.[3], where a commendable review of prior works on beam theory development is given. A characteristic parameter (e.g. the cross-section thickness) is adopted to build an asymptotic series. The terms which exhibit the same order of magnitude as the parameter when it vanishes are retained. This work has been the origin of an alternative approach in formulating refined beam theories, which has led to an extensive contribution in last decade by Volovoi, Hodges, Popescu [58, 47], Yu and co-workers [62, 61] on asymptotic variational methods (VABS). Generalized beam theories originated with Schardt's work [50, 51]. GBT improves classical theories by using a piecewise beam description of thin-walled sections. It has been extensively employed and extended in various forms by Silvestre and co-workers [54, 53, 25].

Many other higher-order theories have been proposed to include non-classical effects based on enhanced displacement fields over the beam cross-section. Some considerations on higher-order beam elements were made by Washizu [59]. Aeroelastic problems of thin-walled beams are considered in the article by Librescu [44]. Giavotto et al.[32] presented an innovative formulation to calculate the stiffness and stresses of a beam section made of anisotropic and non-homogeneous materials via a FE approach. The above literature overview clearly shows the interest in further developments in refined theories for wing structures.

Due to that interest, Carrera and co-authors have recently proposed refined 1D theories with only generalized displacement variables for the analysis of compact and thin-walled sections/airfoils. Higher-order models are obtained in the framework of the Carrera Unified Formulation, CUF. This formulation has been developed over the last decade for plate/shell models [5, 6, 7, 10] and it has recently been extended to beam static and dynamic modeling [11, 12, 15, 16, 14,

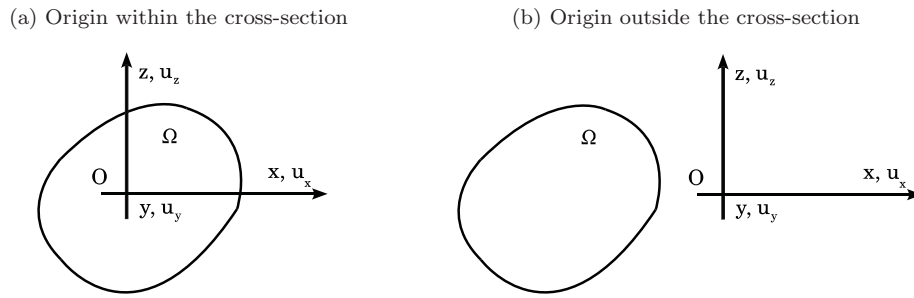


**Figure 1:** Beam's cross-section geometry and coordinate system.

13]. CUF is a hierarchical formulation which considers the order of the model as a free-parameter (i.e. an input) of the analysis. In other words, refined models are obtained with no need for *ad hoc* formulations. Beam theories are obtained on the basis of Taylor-type expansions. Euler-Bernoulli and Timoshenko beam theories are obtained as particular cases of the first-order expansion. The finite element method is used to handle arbitrary geometries as well as geometrical and loading conditions.

The present work couples a refined one-dimensional model based on CUF with the Vortex Lattice Method (VLM) for the analysis of static response of aircraft wings. The computation of linear steady aerodynamic loads refers to the Vortex Lattice Method presented by Katz and Plotkin [42]. The VLM is a 3D, free wake aerodynamic method widely used even in recent static aeroelastic problems [1] and implemented in some free codes such as Tornado and Neo-CASS. It is the steady flow version of the Doublet Lattice Method, an unsteady aerodynamic tool implemented in commercial codes such as MSC Nastran for aeroelastic analysis. The aerodynamic load transfer to the structural mesh is based on the work presented by Demasi and Livne [24, 23] via the Infinite Plate Spline model introduced by Harder et al.[34, 35], and Rodden et al.[49]. The proposed formulation couples the hierarchical one-dimensional structural elements with the Infinite Plate Spline by using the concept of pseudo-structural points. The latter technique could be easily extended to the analysis of static aeroelastic response of lifting surfaces, see Varello et al.[57].

The paper is organized as follows: after the discussion of the theoretical model, several applications on a number of wing configurations are presented. Assessments of both the aerodynamic and structural models are carried out. Due to the high accuracy used to represent the displacement field of the structure, it is concluded that the present model is ideal for aerolastic applications, as inferred in the concluding preliminary aeroelastic study. This work shows how the Vortex Lattice Method is coupled with the proposed advanced beam model, but it is not limited to panel methods: high fidelity CFD codes can be successfully used.

## 2. Preliminaries

A beam is a structure whose axial length  $L$  is predominant with respect to the two other orthogonal dimensions. The intersection of the beam with a plane that is perpendicular to its axis identifies the so-called beam's *cross-section*  $\Omega$ . As shown in Fig. 1, a local cartesian coordinate system composed of  $x$  and  $z$  axes parallel to the cross-section plane is defined, whereas  $y$  represents the out-of-plane coordinate. However, the  $y$  axis is not necessarily a centroidal one. Moreover, the cross-sections are not necessarily perpendicular to the geometric axis of the beam. This gives high versatility to the present structural beam model.  $u_x$ ,  $u_y$ , and  $u_z$  are the cartesian components of the displacement vector:

$$\mathbf{u}(x, y, z) = \left\{ u_x \quad u_y \quad u_z \right\}^T \quad (1)$$

where superscript  $T$  stands for the transposition operator. The stress,  $\boldsymbol{\sigma}$ , and the strain,  $\boldsymbol{\varepsilon}$ , are grouped in vectors as follows:

$$\begin{aligned}\boldsymbol{\sigma}_p &= \left\{ \begin{matrix} \sigma_{zz} & \sigma_{xx} & \sigma_{zx} \end{matrix} \right\}^T & \boldsymbol{\varepsilon}_p &= \left\{ \begin{matrix} \varepsilon_{zz} & \varepsilon_{xx} & \varepsilon_{zx} \end{matrix} \right\}^T \\ \boldsymbol{\sigma}_n &= \left\{ \begin{matrix} \sigma_{zy} & \sigma_{xy} & \sigma_{yy} \end{matrix} \right\}^T & \boldsymbol{\varepsilon}_n &= \left\{ \begin{matrix} \varepsilon_{zy} & \varepsilon_{xy} & \varepsilon_{yy} \end{matrix} \right\}^T\end{aligned}\quad (2)$$

Subscript  $n$  refers to quantities related to the beam cross-section  $\Omega$ , whereas subscript  $p$  refers to quantities related to the out-of-plane direction. In the case of small displacements with respect to the length  $L$ , the linear relations between strain and displacement components hold and a compact vectorial notation can be adopted:

$$\begin{aligned}\boldsymbol{\varepsilon}_p &= \mathbf{D}_p \mathbf{u} \\ \boldsymbol{\varepsilon}_n &= \mathbf{D}_n \mathbf{u} = \mathbf{D}_{np} \mathbf{u} + \mathbf{D}_{ny} \mathbf{u}\end{aligned}\quad (3)$$

where  $\mathbf{D}_p$ ,  $\mathbf{D}_{np}$ , and  $\mathbf{D}_{ny}$  are differential matrix operators:

$$\mathbf{D}_p = \begin{bmatrix} 0 & 0 & \frac{\partial}{\partial z} \\ \frac{\partial}{\partial x} & 0 & 0 \\ \frac{\partial}{\partial z} & 0 & \frac{\partial}{\partial x} \end{bmatrix}, \quad \mathbf{D}_{np} = \begin{bmatrix} 0 & \frac{\partial}{\partial z} & 0 \\ 0 & \frac{\partial}{\partial x} & 0 \\ 0 & 0 & 0 \end{bmatrix}, \quad \mathbf{D}_{ny} = \begin{bmatrix} 0 & 0 & \frac{\partial}{\partial y} \\ \frac{\partial}{\partial y} & 0 & 0 \\ 0 & \frac{\partial}{\partial y} & 0 \end{bmatrix}\quad (4)$$

The generalized Hooke's law for isotropic materials holds:

$$\boldsymbol{\sigma} = \mathbf{C} \boldsymbol{\varepsilon}\quad (5)$$

According to Eq. 2, the previous expression becomes:

$$\begin{aligned}\boldsymbol{\sigma}_p &= \mathbf{C}_{pp} \boldsymbol{\varepsilon}_p + \mathbf{C}_{pn} \boldsymbol{\varepsilon}_n \\ \boldsymbol{\sigma}_n &= \mathbf{C}_{np} \boldsymbol{\varepsilon}_p + \mathbf{C}_{nn} \boldsymbol{\varepsilon}_n\end{aligned}\quad (6)$$

where matrices  $\mathbf{C}_{pp}$ ,  $\mathbf{C}_{pn}$ ,  $\mathbf{C}_{np}$  and  $\mathbf{C}_{nn}$  are:

$$\begin{aligned}\mathbf{C}_{pp} &= \begin{bmatrix} C_{11} & C_{12} & 0 \\ C_{12} & C_{22} & 0 \\ 0 & 0 & C_{44} \end{bmatrix}, & \mathbf{C}_{pn} &= \mathbf{C}_{np}^T = \begin{bmatrix} 0 & 0 & C_{13} \\ 0 & 0 & C_{23} \\ 0 & 0 & 0 \end{bmatrix}, \\ \mathbf{C}_{nn} &= \begin{bmatrix} C_{55} & 0 & 0 \\ 0 & C_{66} & 0 \\ 0 & 0 & C_{33} \end{bmatrix}\end{aligned}\quad (7)$$

For the sake of brevity, the dependence of the coefficients  $C_{ij}$  on Young's moduli, Poisson's ratios, and shear moduli is not reported here. It can be found in Reddy [48] or Jones [38]. In this paper isotropic materials will be considered. The extension to composite beams will be presented in future papers.

### 3. Refined Beam Theory

According to the framework of the Carrera Unified Formulation (CUF) [7, 22], the displacement field is assumed to be an expansion of a certain class of functions  $F_\tau$ , which depend on the cross-section coordinates  $x$  and  $z$ :

$$\mathbf{u}(x, y, z) = F_\tau(x, z) \mathbf{u}_\tau(y) \quad \tau = 1, 2, \dots, N_u = N_u(N) \quad (8)$$

The compact expression is based on Einstein's notation: repeated subscript  $\tau$  indicates summation. The number of expansion terms  $N_u$  depends on the expansion order  $N$ , which is a free parameter of the formulation. Mac Laurin's polynomials are chosen as cross-section functions  $F_\tau$  and are listed in Table 1.

| $N$      | $N_u$                  | $F_\tau$   |
|----------|------------------------|--|
| 0        | 1                      | $F_1 = 1$  |
| 1        | 3                      | $F_2 = x \quad F_3 = z$  |
| 2        | 6                      | $F_4 = x^2 \quad F_5 = xz \quad F_6 = z^2$                                       |
| $\vdots$ | $\vdots$               | $\vdots$   |
| $N$      | $\frac{(N+1)(N+2)}{2}$ | $F_{\frac{(N^2+N+2)}{2}} = x^N \quad \dots \quad F_{\frac{(N+1)(N+2)}{2}} = z^N$ |

**Table 1:** Number of expansion terms and MacLaurin's polynomials as a function of  $N$ .

Most displacement-based theories can be formulated on the basis of the above generic kinematic field. For instance, when  $N = 2$ , the second-order axiomatic displacement field is given by:

$$\begin{aligned}
 u_x &= u_{x1} + u_{x2}x + u_{x3}z + u_{x4}x^2 + u_{x5}xz + u_{x6}z^2 \\
 u_y &= u_{y1} + u_{y2}x + u_{y3}z + u_{y4}x^2 + u_{y5}xz + u_{y6}z^2 \\
 u_z &= u_{z1} + u_{z2}x + u_{z3}z + u_{z4}x^2 + u_{z5}xz + u_{z6}z^2
 \end{aligned} \tag{9}$$

Subsequently, the classical beam models such as Timoshenko's (TBM) [56] and Euler-Bernoulli's (EBBM) [29], are easily derived from the first-order approximation model. Timoshenko's beam model (TBM) can be obtained by setting terms  $\{u_{ij} : i = x, z; j = 2, 3\}$  equal to zero. In addition, an infinite rigidity in the transverse shear is also adopted for EBBM by penalizing  $\varepsilon_{xy}$  and  $\varepsilon_{yz}$  via a high penalty value in the following constitutive equations:

$$\sigma_{yz} = C_{55} \varepsilon_{yz} \qquad \sigma_{xy} = C_{66} \varepsilon_{xy} \tag{10}$$

Higher-order models provide an accurate description of the shear mechanics, the cross-section deformation, Poisson's effect along the spatial directions and the torsional mechanics in more detail than classical models do. EBBM neglects them all, since it was formulated to describe the bending mechanics. TBM accounts for constant shear stress and strain components. Classical theories and first-order models require the assumption of opportunely reduced material stiffness coefficients to correct Poisson's locking effect [8, 9]. According to Carrera and Giunta [11], the same technique is used here to correct Poisson's locking.

#### 4. Finite Element Formulation

Following standard FEM, the unknown variables in the element domain are expressed in terms of their values corresponding to the element nodes [16]. By introducing the shape functions  $N_i$  and the nodal displacement vector  $\mathbf{q}$ , the displacement field becomes:

$$\mathbf{u}(x, y, z) = F_\tau(x, z) N_i(y) \mathbf{q}_{\tau i} \qquad i = 1, 2, \dots, N_N \tag{11}$$

where:

$$\mathbf{q}_{\tau i} = \left\{ q_{u_{x\tau i}} \quad q_{u_{y\tau i}} \quad q_{u_{z\tau i}} \right\}^T \tag{12}$$

contains the degrees of freedom of the  $\tau^{\text{th}}$  expansion term corresponding to the  $i^{\text{th}}$  element node. Elements with  $N_N$  number of nodes equal to 2, 3 and 4 are formulated and named  $B2$ ,  $B3$ , and  $B4$ , respectively. The results reported in the present work involve only  $B4$  elements. For the sake of brevity, more details are not reported here, but can be found in Carrera et al.[12, 15]. This beam model can be easily extended to mixed theories. However, this work presents a displacement-based formulation. The variational statement is then the Principle of Virtual Displacements:

$$\delta L_{int} = \int_V (\delta \varepsilon_n^T \boldsymbol{\sigma}_n + \delta \varepsilon_p^T \boldsymbol{\sigma}_p) dV = \delta L_{ext} \tag{13}$$

where  $\delta L_{int}$  is the internal virtual work and  $\delta L_{ext}$  is the external virtual work. Substituting Eq. 11 into Eq. 3 and using the fact that  $F_\tau$  are independent of  $y$ , the strain vectors can be written as:

$$\begin{aligned}\varepsilon_n &= (\mathbf{D}_{np} F_\tau \mathbf{I}) N_i \mathbf{q}_{\tau i} + F_\tau (\mathbf{D}_{ny} N_i \mathbf{I}) \mathbf{q}_{\tau i} \\ \varepsilon_p &= (\mathbf{D}_p F_\tau \mathbf{I}) N_i \mathbf{q}_{\tau i}\end{aligned}\quad (14)$$

Therefore, the expression of the internal virtual work (Eq. 13) can be rewritten in terms of virtual nodal displacements as follows:

$$\delta L_{int} = \delta \mathbf{q}_{\tau i}^T \mathbf{K}^{ij\tau s} \mathbf{q}_{sj} \quad (15)$$

where Eq. 6 has been used. The  $3 \times 3$  *fundamental nucleus* of the structural stiffness matrix presented in Eq. 15 can be shown to have the following explicit equation:

$$\begin{aligned}\mathbf{K}^{ij\tau s} &= I_l^{ij} \triangleleft (\mathbf{D}_{np}^T F_\tau \mathbf{I}) \left[ \mathbf{C}_{np} (\mathbf{D}_p F_s \mathbf{I}) + \mathbf{C}_{nn} (\mathbf{D}_{np} F_s \mathbf{I}) \right] + \\ &\quad (\mathbf{D}_p^T F_\tau \mathbf{I}) \left[ \mathbf{C}_{pp} (\mathbf{D}_p F_s \mathbf{I}) + \mathbf{C}_{pn} (\mathbf{D}_{np} F_s \mathbf{I}) \right] \triangleright_\Omega + \\ &I_l^{ij,y} \triangleleft \left[ (\mathbf{D}_{np}^T F_\tau \mathbf{I}) \mathbf{C}_{nn} + (\mathbf{D}_p^T F_\tau \mathbf{I}) \mathbf{C}_{pn} \right] F_s \triangleright_\Omega \mathbf{I}_{\Omega y} + \\ &I_l^{i,yj} \mathbf{I}_{\Omega y} \triangleleft F_\tau \left[ \mathbf{C}_{np} (\mathbf{D}_p F_s \mathbf{I}) + \mathbf{C}_{nn} (\mathbf{D}_{np} F_s \mathbf{I}) \right] \triangleright_\Omega + \\ &I_l^{i,yj,y} \mathbf{I}_{\Omega y} \triangleleft F_\tau \mathbf{C}_{nn} F_s \triangleright_\Omega \mathbf{I}_{\Omega y}\end{aligned}\quad (16)$$

where:

$$\mathbf{I}_{\Omega y} = \begin{bmatrix} 0 & 1 & 0 \\ 1 & 0 & 0 \\ 0 & 0 & 1 \end{bmatrix} \quad \triangleleft \dots \triangleright_\Omega = \int_\Omega \dots d\Omega \quad (17)$$

$$\left( I_l^{ij}, I_l^{ij,y}, I_l^{i,yj}, I_l^{i,yj,y} \right) = \int_L \left( N_i N_j, N_i N_{j,y}, N_{i,y} N_j, N_{i,y} N_{j,y} \right) dy \quad (18)$$

The symbol  $\triangleleft \dots \triangleright_\Omega$  indicates integration over the cross section. It should be noted that no assumptions on the expansion order have been made. Therefore, it is possible to obtain refined beam models without changing the formal expression of the nucleus components. The present model is invariant with respect to the order of the beam theory and the type of element used in the finite element axial discretization. Shear locking is corrected through selective integration [2].

## 5. Structural and Aerodynamic Notations

Classical beam models provide acceptable results only for relatively high aspect ratio beams. With the proposed hierarchical beam formulation based on CUF, the accuracy of the axiomatic model can be freely increased. This implies that the present method can be used for relatively small aspect ratio. Therefore, it is an ideal tool to analyze large aspect ratio wings typical of High Altitude Long Endurance vehicles and small aspect ratio wing configurations such as delta wings, see [12, 15, 19]. Moreover, as will be presented in this work, non-planar configurations can be successfully addressed with the present structural beam model.

A global coordinate system  $x-y-z$  is placed on the airfoil's leading edge point at the wing root section. The global  $x$  axis is parallel to the free stream velocity  $\mathbf{V}_\infty$  and directed toward the trailing edge. The global  $z$  axis also lies in the aircraft's plane of symmetry, whereas the  $y$  axis goes along the spanwise direction.

The proposed beam model can easily analyze tapered wings with dihedral and sweep angles. The aerodynamic mesh is on a reference trapezoidal surface with 2 edges parallel to the wind direction. Then a second coordinate system  $x_{loc'}-y_{loc'}-z_{loc'}$  with the same origin as the global one is introduced so that the

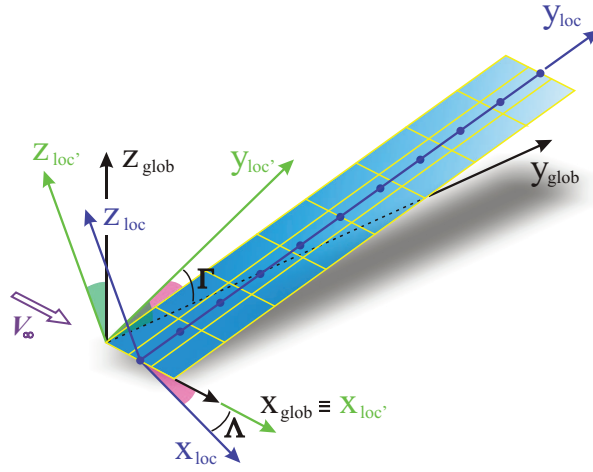


**Figure 2:** One-dimensional structural mesh and two-dimensional aerodynamic mesh of wing segments.

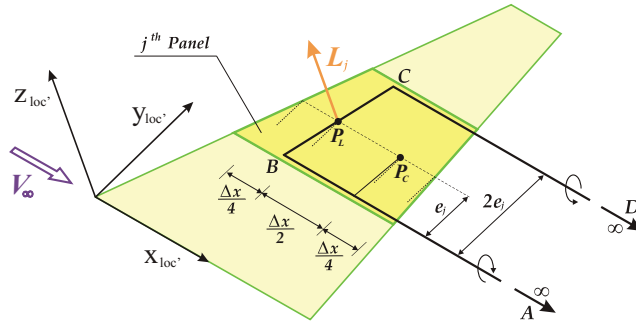


**Figure 3:** The horseshoe convention followed for the VLM.

reference surface lies on the plane  $x_{loc'}-y_{loc'}$ . The  $x_{loc'}$  and  $x$  axes are parallel to  $\mathbf{V}_\infty$  (see Fig. 2).

The wing is modeled with a straight beam. The structural mesh is contained on the trapezoidal reference surface. An additional local coordinate system is used to identify the 1D structural mesh on the beam.  $y_{loc}$  is the axis of the beam (see Fig. 2), whereas  $z_{loc}$  is perpendicular to the trapezoidal surface.

The aerodynamic method here chosen is the Vortex Lattice Method (VLM) [42]. The aerodynamic mesh, which consists in a lattice of  $N_{AP}$  quadrilateral panels, lies on the trapezoidal reference surface. A horseshoe element is placed on each panel and the typical scheme is shown in Fig. 3. The aerodynamic force is applied at the load point  $P_L$ , whereas the wall tangency condition is imposed at the control point  $P_C$ .

## 6. Aerodynamic Load Transfer

The fundamental nucleus (see Eq. 16) was derived in the local coordinate system  $x_{loc}-y_{loc}-z_{loc}$ . For reasons that will appear clear later, the notation is slightly modified to reflect this fact:

$$\delta L_{int} = \delta \mathbf{q}_{\tau i \text{ loc}}^T \mathbf{K}_{\text{loc}}^{ij\tau s} \mathbf{q}_{s j \text{ loc}} \quad (19)$$

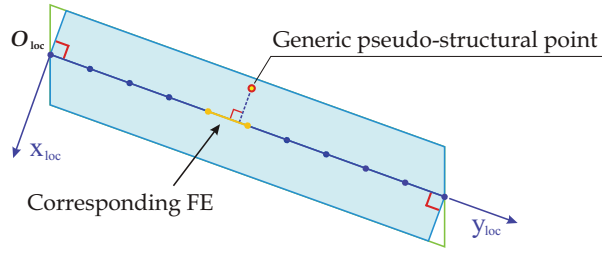
The present capability is aimed at the analysis of generic wing configurations including non-planar joined wings. This requires the writing of the finite element stiffness matrix in the global coordinate system. This can be accomplished by expressing the vector  $\mathbf{q}_{\tau i \text{ loc}}$  of local nodal degrees of freedom in global coordinates as follows:

$$\mathbf{q}_{\tau i \text{ loc}} = \mathbf{e} \cdot \mathbf{q}_{\tau i} \quad (20)$$

where  $\mathbf{e}$  is a  $3 \times 3$  rotation matrix. Substituting Eq. 20 into Eq. 19, the expression of the fundamental nucleus in the global coordinate system is obtained:

$$\delta L_i = \delta \mathbf{q}_{\tau i}^T \left[ \mathbf{e}^T \cdot \mathbf{K}_{\text{loc}}^{ij\tau s} \cdot \mathbf{e} \right] \mathbf{q}_{s j} = \delta \mathbf{q}_{\tau i}^T \mathbf{K}^{ij\tau s} \mathbf{q}_{s j} \quad (21)$$

**Figure 4:** Shaded area on which a set of pseudo-structural points is placed.



The finite element assembly procedure to build  $\mathbf{K}$  enforces the compatibility of the displacements expressed in global coordinates.

### 6.1 Splining and Pseudo-Structural Points

The present advanced beam model allows a very accurate calculation of the displacement field at all points of the three-dimensional wing. Based on this property, it is possible to effectively use the Infinite Plate Spline (IPS) method [34, 20, 63] for the aerodynamic load transferring. The transfer of aerodynamic pressure on the structural nodes requires the displacements at load points to be written in terms of the nodal displacement vector  $\mathbf{q}$ . The spline satisfies this requirement wherever the generic load point  $P_L$  lies on the wing reference surface.

The Infinite Plate Spline method [23, 24, 34] was shown (see [57]) to be the ideal choice for the advanced multi-fidelity beam model presented in this work. The spline technique is here preparatory for the aeroelastic extension of the present work, in which the splining will directly provide the calculation of the local slopes necessary for the interfacing wall-tangency boundary condition. A brief description of the splining procedure is now provided. The coordinate system  $x_{loc'} - y_{loc'} - z_{loc'}$  is used for the splining of a generic trapezoidal surface. A set of  $N_{PS}$  points is chosen in the shaded area shown in Fig. 4. The displacements of these points can be accurately calculated with the advanced beam model and are used for the splining. This set of points is not part of the element structural nodes. However, they are “seen” as structural points in the splining. For that reason, the points on the shaded area are indicated as *pseudo-structural points*. They are not coincident with the finite element nodes.

By defining  $\mathbf{x}$  as the vector containing the global coordinates of pseudo-structural points, their coordinates  $\mathbf{x}_{loc'}$  expressed in the local' reference system are determined by introducing the block diagonal matrix  $\mathbf{E}_\Gamma^{PS}$ , which is a transformation matrix. Similarly, the local coordinates  $\mathbf{x}_{loc}$  are computed by means of a transformation matrix  $\mathbf{E}^{PS}$  and vector  $\mathbf{x}_{O_{loc}}$ , in which the global coordinates of the origin point  $O_{loc}$  are repeated as many times as  $N_{PS}$ :

$$\mathbf{x}_{loc'} = \mathbf{E}_\Gamma^{PS} \cdot \mathbf{x} \quad \mathbf{x}_{loc} = \mathbf{E}^{PS} \cdot (\mathbf{x} - \mathbf{x}_{O_{loc}}) \quad (22)$$

The nodal displacement vector  $\mathbf{q}$  in global coordinates can be referred to the local coordinate system (see Eq. 20) by using a transformation matrix  $\mathbf{E}$  as follows:

$$\mathbf{q}_{loc} = \mathbf{E} \cdot \mathbf{q} \quad (23)$$

To compute the displacement of each pseudo-structural point it is necessary to identify which finite element has to be associated with the given pseudo-structural point. This is accomplished by calculating the local coordinate  $y_{loc}$  from vector  $\mathbf{x}_{loc}$  and by selecting the corresponding finite element as shown in Fig. 4. Everything is expressed in local coordinates, thus the FEM equation 11 can be used to calculate the local displacement of the generic pseudo-structural point according to CUF. By using Eq. 23 again, it is useful to define a matrix  $\mathbf{Y}$  which relates the vector of nodal DOFs expressed in local coordinates with the displacements  $\hat{\mathbf{u}}_{loc}$  (in local coordinates) of all the pseudo-structural points.

Thus, calling  $\mathbf{I}_z$  the constant matrix which allows the extraction of  $z_{loc}$  component of the local displacements and noting that  $z_{loc}$  and  $z_{loc'}$  axes are parallel, Eq. 24 can be formulated:

$$\mathbf{Z}_{loc'} = \mathbf{Z}_{loc} = \mathbf{I}_z \cdot \hat{\mathbf{u}}_{loc} = \mathbf{I}_z \cdot \mathbf{Y} \cdot \mathbf{q}_{loc} = \mathbf{I}_z \cdot \mathbf{Y} \cdot \mathbf{E} \cdot \mathbf{q} \quad (24)$$

Vector  $\mathbf{Z}_{loc'}$  contains the local' transverse coordinates of pseudo-structural points in the *deformed* configuration and so the input data for the spline method. By using the fitted surface spline it is possible to calculate the  $z_{loc'}$  coordinate of any point lying on this shape. This also applies to load points placed in the not shaded area (Fig. 4).

In this paper both the aerodynamics and the structure are analyzed with linear models. Linearity implies that the displacements are small. Consequence of this assumption is that the local' in-plane coordinates do not change even if the structure deforms. In other words, the splining matrices are constant and can be calculated once.

According to the IPS method, the  $Z_{i loc'}$  for the corresponding  $i^{\text{th}}$  pseudo-structural point is written as:

$$Z_{i loc'} = a_0 + a_1 x_{i loc'} + a_2 y_{i loc'} + \sum_{j=1}^{N_{PS}} \hat{F}_j \hat{K}_{ij} \quad (25)$$

where:

$$\hat{K}_{ij} = (r_{ij loc'})^2 \ln(r_{ij loc'})^2 \quad (26)$$

$$(r_{ij loc'})^2 = (x_{i loc'} - x_{j loc'})^2 + (y_{i loc'} - y_{j loc'})^2 \quad (27)$$

For the sake of brevity, the details about the IPS method [34, 20] are not reported here. By writing Eq. 25 for all the pseudo-structural points, it can be shown that the following matrix notation is obtained:

$$\mathbf{Z}_{loc'}^* = \begin{bmatrix} \mathbf{0} & \mathbf{R} \\ \mathbf{R}^T & \hat{\mathbf{K}} \end{bmatrix} \cdot \mathbf{P} = \mathbf{G} \cdot \mathbf{P} \quad (28)$$

Vector  $\mathbf{Z}_{loc'}^*$  is coincident with  $\mathbf{Z}_{loc'}$  except for the fact that three zero rows are added [63]. By inverting Eq. 28, it is possible to find the  $N_{PS} + 3$  components of vector  $\mathbf{P}$ . The components represent the spline coefficients  $a_0$ ,  $a_1$ ,  $a_2$ , and  $\hat{F}_j$ s.

The equation of the spline can be used to calculate the displacements at any selected point and therefore to compute the equivalent nodal aerodynamic forces. The next phase will show how to transform lift forces at aerodynamic load points into equivalent nodal forces on the structural grid. This transformation will involve the displacements of load points. Let  $(\tilde{\mathcal{X}}_{k loc'}, \tilde{\mathcal{Y}}_{k loc'})$  be the local' coordinates of the  $k^{\text{th}}$  load point. Its coordinate along the  $z_{loc'}$  axis is given by:

$$\tilde{\mathcal{Z}}_{k loc'} = a_0 + a_1 \tilde{\mathcal{X}}_{k loc'} + a_2 \tilde{\mathcal{Y}}_{k loc'} + \sum_{j=1}^{N_{PS}} \hat{F}_j \tilde{\mathcal{K}}_{kj} \quad (29)$$

where:

$$\tilde{\mathcal{K}}_{kj} = (\tilde{\mathcal{R}}_{kj loc'})^2 \ln(\tilde{\mathcal{R}}_{kj loc'})^2 \quad (30)$$

$$(\tilde{\mathcal{R}}_{kj loc'})^2 = (\tilde{\mathcal{X}}_{k loc'} - x_{j loc'})^2 + (\tilde{\mathcal{Y}}_{k loc'} - y_{j loc'})^2 \quad (31)$$

Following the presented procedure for all the  $N_{AP}$  load points, their displacements can be written as functions of the spline coefficients in a compact form:

$$\tilde{\mathcal{Z}}_{loc'} = \tilde{\mathcal{D}}^* \cdot \mathbf{P} \quad (32)$$

An expression that directly relates the local' transverse coordinates of the load points to the local' transverse coordinates of the pseudo-structural points can be obtained by substituting Eq. 28 into Eq. 32:

$$\tilde{\mathcal{Z}}_{loc'} = \tilde{\mathcal{D}}^* \cdot \mathbf{P} = \tilde{\mathcal{D}}^* \cdot \mathbf{G}^{-1} \cdot \mathbf{Z}_{loc'}^* = \tilde{\mathcal{D}}^* \cdot \mathbf{S} \cdot \mathbf{Z}_{loc'} \quad (33)$$

where  $\mathbf{G}^{-1}$  is the inverse matrix of  $\mathbf{G}$ . The matrix  $\mathbf{S}$  is the  $(N_{PS} + 3) \times N_{PS}$  matrix obtained from  $\mathbf{G}^{-1}$  by eliminating the first three columns, since the first three rows of  $\mathbf{Z}_{loc}^*$  are zero. Finally by combining Eqs. 24 and 33, the following expression relates the displacement vector at load points to the vector of nodal degrees of freedom of the whole structure:

$$\tilde{\mathbf{Z}}_{loc'} = \tilde{\mathbf{D}}^* \cdot \mathbf{S} \cdot \mathbf{I}_z \cdot \mathbf{Y} \cdot \mathbf{E} \cdot \mathbf{q} = \tilde{\mathbf{A}}_3^* \cdot \mathbf{q} \quad (34)$$

## 6.2 Steady Aerodynamic Forces

The derivation of aerodynamic loads is now faced. According to the Vortex Lattice Method [42], the pressures acting on the wing are transferred as lift forces located on load points of the aerodynamic panels. Considering the dimensionless pressure  $\Delta p_j$  acting on the generic  $j^{\text{th}}$  panel, the modulus of the lift force applied at the corresponding load point is given by:

$$L_j = \frac{1}{2} \rho_\infty V_\infty^2 \Delta x_j 2e_j \Delta p_j \quad (35)$$

where the quantity  $\Delta x_j$  is the average chord of the panel and  $e_j$  refers to its half-length along the  $y_{loc'}$  axis (wing spanwise direction, see Fig. 3). Since the reference aerodynamic configuration has no angle of attack, it should be noted that lift forces are perpendicular both to the panels and to the wind direction. Let  $\Delta \mathbf{p}$  be the vector containing the dimensionless pressure loads acting on all the aerodynamic panels of the structure, normalized with respect to the dynamic pressure. The lift forces moduli are written in matrix form:

$$\mathbf{L} = \frac{1}{2} \rho_\infty V_\infty^2 \mathbf{I}^D \cdot \Delta \mathbf{p} \quad (36)$$

where  $\mathbf{I}^D$  contains the panels' geometrical data. The VLM allows the dimensionless normalwash, normalized with respect to  $V_\infty$ , to be described as a function of the pressures acting on each aerodynamic panel:

$$\mathbf{w} = \mathbf{A}^D \cdot \Delta \mathbf{p} \quad (37)$$

where  $\mathbf{A}^D$  is the Aerodynamic Influence Coefficient Matrix. It is calculated using the geometrical data of the aerodynamic mesh. The wall tangency condition is imposed at the control point of each panel by setting the dimensionless normalwash to be equal to the local slope.

$$w = \tan(\pi - \alpha) \quad (38)$$

where the angle of attack  $\alpha$  is a small quantity (linear aerodynamic model). Combining Eqs. 37 - 38 and substituting in Eq. 36, the vector containing the aerodynamic forces is written as a function of nodal DOFs:

$$\begin{aligned} \mathbf{L} &= \frac{1}{2} \rho_\infty V_\infty^2 \mathbf{I}^D \cdot [\mathbf{A}^D]^{-1} \cdot \mathbf{w} \\ &= \frac{1}{2} \rho_\infty V_\infty^2 \tan(\pi - \alpha) \mathbf{I}^D [\mathbf{A}^D]^{-1} \mathbf{d} = \frac{1}{2} \rho_\infty V_\infty^2 \tan(\pi - \alpha) \bar{\mathbf{b}} \end{aligned} \quad (39)$$

where  $\mathbf{d}$  stands for a  $N_{AP} \times 1$  vector of ones and  $\bar{\mathbf{b}} = \mathbf{I}^D [\mathbf{A}^D]^{-1} \mathbf{d}$ .

The aerodynamic loads  $\mathbf{L}$  of Eq. 39 are concentrated forces applied at the load points of the aerodynamic panels. They are transformed into *energetically* equivalent nodal loads by the following algorithm. All the lift forces are parallel to the  $z_{loc'}$  axis (see Fig. 3). The transfer of loads at the aerodynamic points to the energetically equivalent loads at structural nodes is performed via the Principle of Virtual Displacements. The work done by the aerodynamic forces

(vector  $\mathbf{L}$ ) applied at the load points is equated to the work done by the equivalent nodal forces (right hand side vector  $\mathbf{L}_{\text{RHS}}$ ). Using Eq. 34 it is possible to write:

$$\begin{aligned} \delta W &= \delta \tilde{\mathbf{z}}_{\text{loc}}^T \cdot \mathbf{L} = \left\{ \tilde{\mathbf{A}}_3^* \cdot \delta \mathbf{q} \right\}^T \cdot \mathbf{L} = \delta \mathbf{q}^T \cdot \tilde{\mathbf{A}}_3^{*T} \cdot \mathbf{L} = \delta \mathbf{q}^T \cdot \mathbf{L}_{\text{RHS}} \\ &\Rightarrow \mathbf{L}_{\text{RHS}} = \tilde{\mathbf{A}}_3^{*T} \cdot \mathbf{L} \end{aligned} \quad (40)$$

where the virtual variation of nodal degrees of freedom  $\mathbf{q}$  is considered. By using Eq. 39, the vector of nodal forces energetically equivalent to the aerodynamic loads can be written as:

$$\mathbf{L}_{\text{RHS}} = \tilde{\mathbf{A}}_3^{*T} \cdot \mathbf{L} = \frac{1}{2} \rho_\infty V_\infty^2 \tan(\pi - \alpha) \tilde{\mathbf{A}}_3^{*T} \cdot \bar{\mathbf{b}} \quad (41)$$

In conclusion, the nodal displacement vector  $\mathbf{q}$  can be computed by solving the linear system:

$$\mathbf{K} \cdot \mathbf{q} = \mathbf{L}_{\text{RHS}} \quad (42)$$

where  $\mathbf{K}$  is the structural stiffness matrix built by Eqs. 16 and 21. For the structural problem, it should be noticed that  $\mathbf{L}_{\text{RHS}}$  does not depend on the nodal displacement vector  $\mathbf{q}$ . The aeroelastic extension of the formulation will take a wall-tangency boundary condition (Eq. 38) depending on the deflection  $\mathbf{q}$  into account. Hence, the aerodynamic loads due to the deformed configuration will lead to the aeroelastic stiffness matrix [57].

## 7. Results and Discussion

Several conventional wing configurations are analyzed in this work and the results are presented here. They are subjected to aerodynamic, bending, and torsional loadings. Cantilever boundary condition is accounted for. For all cases aluminium is considered (Young's modulus  $E = 69$  [GPa] and Poisson's ratio  $\nu = 0.33$ ). The air density is assumed to be  $\rho_\infty = 1.225$  [kg/m<sup>3</sup>].

The wing shapes examined in this work are summarized in Table 2. The first beam is named configuration *A* and consists of a swept tapered wing. The aspect ratio  $AR$  is defined as the square of the wingspan  $b$  divided by the area of the wing planform  $S_w$  and is equal to 10 for configuration *A*. Thus its half-wing corresponds to a cantilever beam which has a span-to-mean chord ratio  $L/\bar{c}$  equal to 5. Configuration *B* has the same value for  $L/\bar{c}$ , but is straight with a taper ratio  $\lambda$  equal to 1. A slender wing is introduced and named configuration *C*. Essentially, its geometry is analogous to configuration *B*, with the only difference of a higher value for the parameter  $L/\bar{c}$ . Wing *D* is dihedral with a taper ratio equal to 0.25 as in the swept configuration *A*, whereas the parameter  $L/\bar{c}$  is higher. Configuration *E* is a forward swept wing with the same properties as those of configuration *A*, with an opposite sweep angle (negative). Last wing, which is named with letter *F*, has the same geometry as configurations *A* and *E*, with the sole difference of a null sweep angle. A further flat plate configuration will be afterwards involved and detailed for the aeroelastic response study.

The beam-like structures are considered to have an airfoil-shaped section or a thin-walled rectangular cross-section. With the exception of configuration *D*, the NACA 2415 airfoil is adopted as cross-section profile, which is subdivided into three cells. The cells are obtained by inserting two spars along the span-wise direction at 25% and 75% of the chord length, see Fig. 5a. Their thicknesses are, respectively, 10% and 7% of the maximum airfoil thickness, whereas the percentage is about 4% for the skin. Configuration *D* has the thin-walled rectangle shown in Fig. 5b as cross-section. The thickness of the skin is 5% of the rectangle's height. The considered height-to-chord length ratio is 0.1.

**Table 2:** Wing configurations adopted to discuss the results.

| Name                    | A       | B       | C       | D        | E       | F       |
|-------------------------|---------|---------|---------|----------|---------|---------|
| Section                 | Airfoil | Airfoil | Airfoil | Wing box | Airfoil | Airfoil |
| $\Lambda$               | + 13.5° | 0°      | 0°      | 0°       | - 13.5° | 0°      |
| $\Gamma$                | 0°      | 0°      | 0°      | 10°      | 0°      | 0°      |
| $\lambda$               | 0.25    | 1       | 1       | 0.25     | 0.25    | 0.25    |
| $c_{root}$ [m]          | 1.6     | 1       | 0.2     | 1.6      | 1.6     | 1.6     |
| $c_{tip}$ [m]           | 0.4     | 1       | 0.2     | 0.4      | 0.4     | 0.4     |
| $\bar{c}$ [m]           | 1       | 1       | 0.2     | 1        | 1       | 1       |
| $L$ [m]                 | 5       | 5       | 4       | 7        | 5       | 5       |
| $L/\bar{c}$             | 5       | 5       | 20      | 7        | 5       | 5       |
| $b$ [m]                 | 10      | 10      | 8       | 14       | 10      | 10      |
| $S_w$ [m <sup>2</sup> ] | 10      | 10      | 1.6     | 14       | 10      | 10      |
| $AR$                    | 10      | 10      | 40      | 14       | 10      | 10      |

Airfoil: NACA 2415 airfoil with 3 cells.

Wing box: thin-walled rectangular cross-section.

 $\Lambda$ : sweep angle $\Gamma$ : dihedral angle $\lambda$ : taper ratio $\bar{c}$ : mean chord $L$ : beam's length $b$ : wingspan $S_w$ : wing area $AR$ : aspect ratio**Figure 5:** Cross-sections used for the wing configurations.

(a) NACA 2415 with 3 cells



(b) Thin-walled rectangle

**Table 3:** Effect of  $V_\infty$  and  $\alpha$  on  $u_{z \max}$ . Configuration A. Aerodynamic mesh:  $4 \times 40$  panels.

|                    | Theory : $N = 3$    | 20 B4 elements | $4 \times 40$ panels |        |        |
|--------------------|---------------------|----------------|----------------------|--------|--------|
| $V_\infty$ [m/s]   | 30                  | 40             | 50                   | 60     | 70     |
| $\alpha = 1^\circ$ | 0.4179 <sup>a</sup> | 0.7429         | 1.1608               | 1.6716 | 2.2753 |
| $\alpha = 5^\circ$ | 2.0946              | 3.7238         | 5.8184               | 8.3785 | 11.404 |

<sup>a</sup> Maximum displacement  $u_{z \max}$  [mm]

## 7.1 Aerodynamic Model Assessment

The first assessment examines the aerodynamic implications closely related to the Vortex Lattice formulation. Wing configuration *A* is discretized by 20 refined *B4* elements and an aerodynamic mesh composed of  $4 \times 40$  panels is set on the surface of the structure. The angle of attack  $\alpha$  of the wing and the free stream velocity  $V_\infty$  are considered as free parameters of the first analysis. The former ranges from 30 to 70 [m/s], whereas the latter varies from  $1^\circ$  to  $5^\circ$ . The effect of such parameters on the maximum displacement  $u_{z \max}$  is investigated and shown in Table 3, where the expansion order is  $N = 3$ .

The quantities  $\alpha$  and  $V_\infty$  affect the pressure distribution and the deflection of the wing only in value, but not in shape. The trend of  $u_{z \max}$  confirms the correlation of the Lift Forces with  $\tan(\pi - \alpha)$  and the square of  $V_\infty$  as expressed in Eq. 39. As in the following analyses, the symmetry condition is exploited in the aerodynamic computation and the cantilever right half-wing of the structure is considered.

The second analysis investigates the pressure distribution on a wing. In order to check the VLM implementation, an assessment with two reference swept configurations is faced. A back-swept wing with  $\Lambda = 45^\circ$  and a forward swept wing with  $\Lambda = -45^\circ$  are considered [42]. The span-to-mean chord ratio  $L/\bar{c}$  is equal to 2 and the terms  $C_l$  and  $C_L$  are introduced as follows:

$$C_l(y) = \frac{L^*(y)}{\frac{1}{2} \rho_\infty V_\infty^2 2e(y)c(y)} \quad C_L = \frac{L_{\text{tot}}}{\frac{1}{2} \rho_\infty V_\infty^2 \frac{b\bar{c}}{2}} \quad (43)$$

where  $c(y)$  and  $L^*(y)$  are the chord and the Lift Force generated by the pressure acting on the panels with span-length  $2e(y)$  placed at the  $y$  coordinate.  $L_{\text{tot}}$  is the Total Lift Force acting on the right half-wing. The trend of the  $\frac{C_l}{C_L}$  ratio along the  $y$  axis is shown for both the swept wings in Fig. 6. In the computation two different aerodynamic meshes are involved, differing in shape and in the total number of panels. It is interesting to note the effect of the sweep angle  $\Lambda$  on the pressure distribution along the spanwise direction. A slight dependence on the aerodynamic mesh used is furthermore detected and notable mainly for the back-swept case. An excellent agreement with the results obtained by Katz and Plotkin [42] is achieved. For the straight configuration *B* it has been verified that the maximum pressure acts on the leading edge of each section, with an overall maximum placed on the root cross-section. The pressure distribution decreases as  $y$  increases according to the low-speed aerodynamics of aircraft straight wings [42].

The third analysis focuses on the effect on the results of the aerodynamic mesh in shape and refinement. Configuration *B* is discretized via a uniform lattice of panels with a variable *panel ratio* (PR). The panel ratio is a parameter defined as the ratio between the chordwise and spanwise lengths of the aerodynamic elements used. In other words, it represents the mesh shape. The Total Lift Force  $L_{\text{tot}}$  and the Total Aerodynamic Moment  $M_{\text{tot}}$  with respect to the quarter chord line acting on the right half-wing as the number of panels changes is reported in Table 4. It is interesting to note that the results are different according to the panels' aspect ratio. For instance, considering panel ratio as equal to 0.5 and panel ratio as equal to 2.0 with the same  $N_{AP} = 40$ , the aerodynamic loadings differ. The same situation recurs for  $N_{AP} = 160$ . As expected, the convergent trend for the VLM is verified for every panel ratio.

## 7.2 Structural Model Assessment

The fourth assessment of the present work discusses the effect of the structural parameters for the first four wings listed in Table 2 undergoing an aerodynamic load.

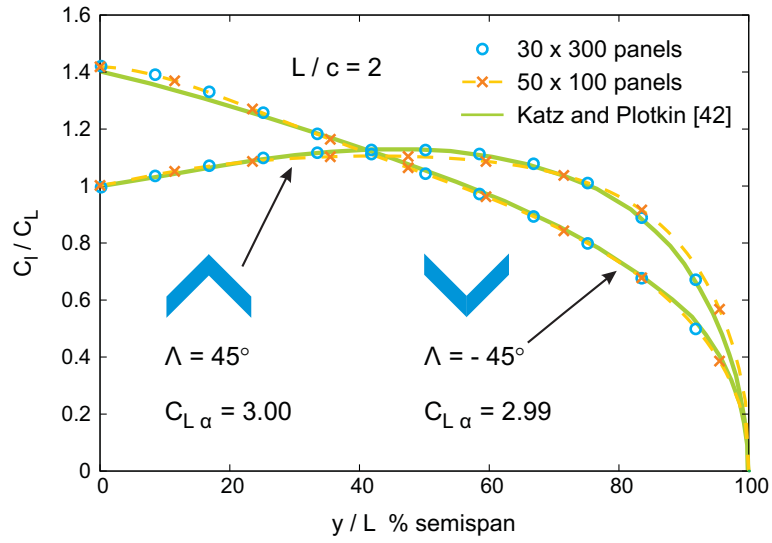


**Figure 6:** Effect of the sweep angle on the spanwise loading for two reference untapered wings.

**Table 4:** Convergence study: Effect of the aerodynamic mesh on Total Lift Force and Total Aerodynamic Moment. Configuration *B*.

| Panel ratio | $V_\infty = 50 \text{ m/s}$   |         | $\alpha = 3 \text{ deg}$ |         | Theory : $N = 3$ |  | 20 B4 el. |  |
|-------------|-------------------------------|---------|--------------------------|---------|------------------|--|-----------|--|
|             | Number of panels along x axis |         |                          |         |                  |  |           |  |
|             | 2                             | 4       | 6                        | 8       | 10               |  |           |  |
| 0.5         | (10) <sup>a</sup>             | (40)    | (90)                     | (160)   | (250)            |  |           |  |
|             | 2039.1 <sup>b</sup>           | 1995.9  | 1979.2                   | 1970.4  | 1965.0           |  |           |  |
|             | -516.86 <sup>c</sup>          | -758.85 | -835.90                  | -873.62 | -895.97          |  |           |  |
| 1.0         | (20)                          | (80)    | (180)                    | (320)   | (500)            |  |           |  |
|             | 1994.7                        | 1970.1  | 1961.2                   | 1956.6  | 1953.8           |  |           |  |
|             | -506.98                       | -749.77 | -828.70                  | -867.75 | -891.04          |  |           |  |
| 2.0         | (40)                          | (160)   | (360)                    | (640)   | (1000)           |  |           |  |
|             | 1968.4                        | 1956.1  | 1951.7                   | 1949.4  | 1948.0           |  |           |  |
|             | -500.78                       | -744.69 | -824.83                  | -864.65 | -888.47          |  |           |  |

<sup>a</sup> (Total number of panels  $N_{AP}$ )  
<sup>b</sup> Total Lift Force  $L_{tot}$  [N]  
<sup>c</sup> Total Aerodynamic Moment  $M_{tot}$  [Nm]

| $V_\infty = 50 \text{ m/s}$ $\alpha = 3 \text{ deg}$ $4 \times 40 \text{ panels}$ |          |          |          |          |          |          |
|---|----------|----------|----------|----------|----------|----------|
| $N_{EL}$  | EBBM     | TBM      | $N = 1$  | $N = 2$  | $N = 3$  | $N = 4$  |
| 2   | 8.8021   | 8.8119   | 8.8189   | 8.2425   | 8.3508   | 8.3686   |
| 5   | 8.8021   | 8.8119   | 8.8189   | 8.4300   | 8.5586   | 8.5805   |
| 10  | 8.8021   | 8.8119   | 8.8189   | 8.4880   | 8.6202   | 8.6431   |
| 20  | 8.8021   | 8.8119   | 8.8189   | 8.5159   | 8.6485   | 8.6723   |
| 40  | 8.8021   | 8.8119   | 8.8189   | 8.5285   | 8.6607   | 8.6854   |
|   | +1.451 % | +1.564 % | +1.645 % | -1.702 % | -0.179 % | +0.106 % |

Nastran (solid - sol 101): 8.6762

**Table 5:** Convergence study: Effect of the number of  $B4$  elements on  $u_{z \max}$  [mm] for different beam models. Configuration  $B$ .

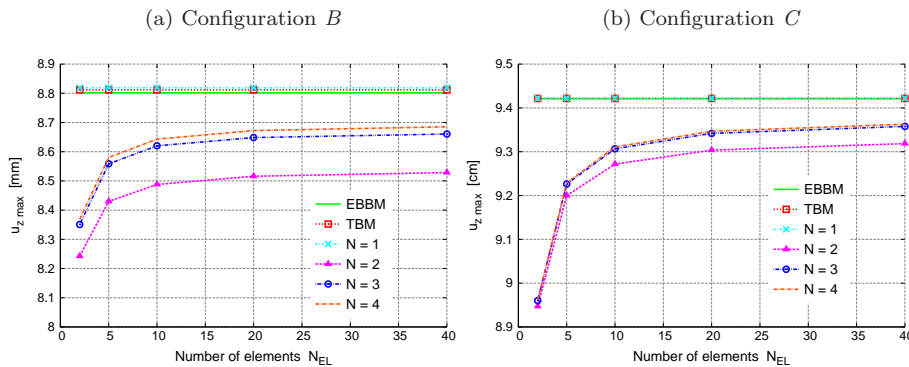


**Figure 7:** Maximum transverse displacement  $u_{z \max}$  as a function of the structural mesh and the models involved for straight wings.

Configuration  $B$  rotated with an angle of attack  $\alpha = 3^\circ$  and exposed to a free stream with  $V_\infty = 50$  [m/s] is considered. Referring to Table 4, the aerodynamic mesh used is fixed to  $4 \times 40$  panels, since it offers both accuracy and low computational cost. A structural convergence study is carried out to evaluate the combined effect of the number of Finite Elements  $N_{EL}$  and the expansion order  $N$  on the solution. The mechanics of the beam is described in terms of the maximum vertical displacement  $u_{z \max}$ , which is located at the leading edge of the tip cross-section for configuration  $B$ . This location derives from the coupling of bending and torsional loads applied on the wing exposed to the free stream. The results are summarized in Table 5.

The maximum displacement increases and becomes more accurate as  $N_{EL}$  increases. Therefore a higher number of elements enhances the flexibility of the structure. The trend is convergent for each adopted theory as reported in Fig. 7a. In particular, when the theory is linear (EBBM, TBM and  $N = 1$ ), the results are not affected by  $N_{EL}$  whereas for  $N > 1$  the solution approaches a reference value.

As far as the approximation order is concerned, the linear theories give very similar results, which are slightly different in the third significant digit. The absolute value of the gap among  $N \geq 1$  theories is more evident underlining the importance of increasing  $N$  to reach convergent results. However, this gap decreases in absolute value as the expansion order increases. Higher orders than linear approximation yield a more flexible structure. It is interesting to note how  $u_{z \max}$  decreases when the theory changes from a linear to a parabolic form. The main reason for this turnaround stands in Poisson's locking correction adopted only for  $N = 1$  [8, 9].

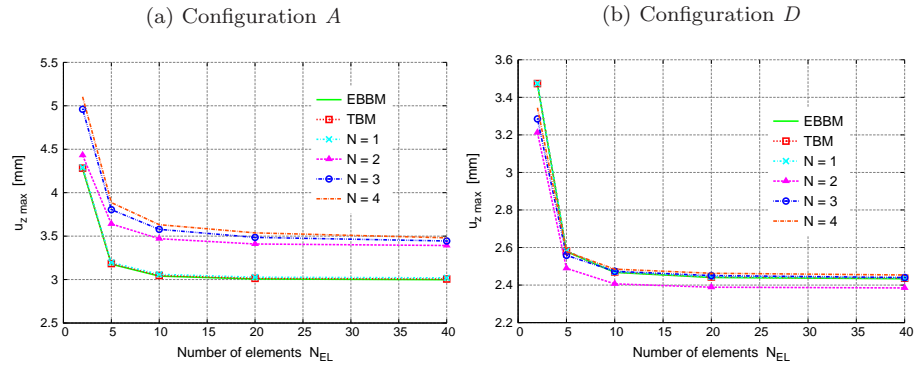
Table 5 also shows the percentage error in computing the maximum displacement for all the theories and a mesh of 40 elements with respect to the reference Nastran solution. A linear static analysis (sol 101) is performed by Nastran. A solid elements model with about  $10^6$  DOFs is used, whereas for the proposed model the maximum number of DOFs involved is equal to 5445 (40 elements,  $N = 4$ ). The aerodynamic loads are placed as concentrated forces on the upper

**Table 6:** Convergence study: Effect of the number of  $B4$  elements on  $u_{z \max}$  [cm] for different beam models. Configuration  $C$ .

|          | $V_\infty = 20 \text{ m/s}$ |          | $\alpha = 3 \text{ deg}$ |          | $4 \times 40 \text{ panels}$ |          |
|----------|-----------------------------|----------|--------------------------|----------|------------------------------|----------|
| $N_{EL}$ | EBBM                        | TBM      | $N = 1$                  | $N = 2$  | $N = 3$                      | $N = 4$  |
| 2        | 9.4210                      | 9.4216   | 9.4220                   | 8.9471   | 8.9603                       | 8.9615   |
| 5        | 9.4210                      | 9.4216   | 9.4220                   | 9.1999   | 9.2263                       | 9.2291   |
| 10       | 9.4210                      | 9.4216   | 9.4220                   | 9.2718   | 9.3067                       | 9.3108   |
| 20       | 9.4210                      | 9.4216   | 9.4220                   | 9.3036   | 9.3418                       | 9.3466   |
| 40       | 9.4210                      | 9.4216   | 9.4220                   | 9.3186   | 9.3578                       | 9.3628   |
|          | +1.046 %                    | +1.052 % | +1.056 %                 | -0.053 % | +0.368 %                     | +0.422 % |

Nastran (solid - sol 101): 9.3235

**Figure 8:** Maximum transverse displacement  $u_{z \max}$  as a function of the structural mesh and the models involved for tapered wings.



surface of configuration  $B$ . An excellent agreement is obtained between Nastran and the higher-order model's results.

Analysis of the combined convergence is carried out also for configuration  $C$  and the conclusions are analogous to the previous case, see Table 6. The free stream velocity is 20 [m/s] in order to avoid large deflections. The convergent trend of  $u_{z \max}$  as  $N_{EL}$  increases is shown in Fig. 7b and is very similar to that obtained for configuration  $B$ .

As far as expansion order is concerned, the results highlight a similar behavior. Nevertheless, by decreasing  $L/\bar{c}$  the use of higher-order theories becomes more and more important. For configuration  $C$  less remarkable differences have been found in the case  $N > 1$  with respect to configuration  $B$ . Cubic and fourth-order approximations differ in the fourth significant digit. Since the first-order approximation matches the classical models, the shear effect and hence the linear terms of  $u_x$  and  $u_z$  for  $N = 1$  can be neglected for this slender beam. It should be noted that EBBM is stiffer than TBM: +0.111% for shorter configuration  $B$  versus +0.006% for slender configuration  $C$ . On the contrary, EBBM is more deformable than  $N = 4$ : -1.344% for shorter configuration  $B$  versus -0.622% for slender configuration  $C$ . An excellent agreement with Nastran is again obtained by higher-order models.

The fourth assessment continues focusing now on two tapered structures. The first is configuration  $A$ , which is discretized by  $4 \times 40$  aerodynamic panels and exposed to  $V_\infty = 50$  [m/s] with  $\alpha = 3^\circ$ . Table 7 summarizes the corresponding results and Fig. 8a shows the trends as the number of elements changes for each theory involved. For any mesh  $u_{z \max}$  increases with  $N$ , to such an extent that no remarkable differences are detected for high-order expansion. As will be clear in the following, this swept wing is subjected to a significant twist of the cross-section. Bearing in mind that linear theories (EBBM, TBM, and  $N = 1$ ) are not able to handle this mechanical behavior, the Poisson's locking correction is not sufficient to make them effective in computing the maximum displacement. On the contrary, the refined models approach Nastran results.

In relation to the numerical convergence, the trend is different with respect

| $V_\infty = 50 \text{ m/s}$ |          | $\alpha = 3 \text{ deg}$ |          | $4 \times 40 \text{ panels}$ |          |          |
|-----------------------------|----------|--------------------------|----------|------------------------------|----------|----------|
| $N_{EL}$                    | EBBM     | TBM                      | $N = 1$  | $N = 2$                      | $N = 3$  | $N = 4$  |
| 2                           | 4.2749   | 4.2829                   | 4.2909   | 4.4309                       | 4.9598   | 5.1036   |
| 5                           | 3.1768   | 3.1842                   | 3.1965   | 3.6408                       | 3.8045   | 3.8858   |
| 10                          | 3.0401   | 3.0473                   | 3.0605   | 3.4701                       | 3.5785   | 3.6316   |
| 20                          | 3.0071   | 3.0144                   | 3.0277   | 3.4097                       | 3.4854   | 3.5377   |
| 40                          | 2.9990   | 3.0062                   | 3.0196   | 3.3920                       | 3.4440   | 3.4802   |
|                             | -13.69 % | -13.49 %                 | -13.10 % | -2.383 %                     | -0.886 % | +0.155 % |

Nastran (solid - sol 101): 3.4748

| $V_\infty = 50 \text{ m/s}$ |          | $\alpha = 3 \text{ deg}$ |          | $4 \times 40 \text{ panels}$ |          |          |
|-----------------------------|----------|--------------------------|----------|------------------------------|----------|----------|
| $N_{EL}$                    | EBBM     | TBM                      | $N = 1$  | $N = 2$                      | $N = 3$  | $N = 4$  |
| 2                           | 3.4704   | 3.4732                   | 3.4744   | 3.2120                       | 3.2852   | 3.3446   |
| 5                           | 2.5787   | 2.5812                   | 2.5822   | 2.4893                       | 2.5586   | 2.5777   |
| 10                          | 2.4675   | 2.4699                   | 2.4709   | 2.4065                       | 2.4733   | 2.4849   |
| 20                          | 2.4407   | 2.4431                   | 2.4441   | 2.3885                       | 2.4508   | 2.4629   |
| 40                          | 2.4340   | 2.4365                   | 2.4374   | 2.3848                       | 2.4404   | 2.4539   |
|                             | -1.282 % | -1.180 %                 | -1.144 % | -3.277 %                     | -1.022 % | -0.474 % |

Nastran (solid - sol 101): 2.4656

**Table 7:** Convergence study: Effect of the number of  $B4$  elements on  $u_{z \max}$  [mm] for different beam models. Configuration  $A$ .

**Table 8:** Convergence study: Effect of the number of  $B4$  elements on  $u_{z \max}$  [mm] for different beam models. Configuration  $D$ .

to configurations  $B$  and  $C$ , since the deflection decreases as  $N_{EL}$  increases. By discretizing the tapered wing with a coarse mesh, the elements close to the tip have cross-sections with dimensions shorter than reality. This leads the analysis to underestimate the moment of inertia and therefore structural stiffness too. This is why the trends of  $u_{z \max}$  versus  $N_{EL}$  for EBBM, TBM, and  $N = 1$  are no longer independent of  $N_{EL}$ . In the case of a swept untapered wing, such curves would have been as straight as for configurations  $B$  and  $C$ . Hence, the taper ratio causes a remarkable difference on the maximum displacement between  $N_{EL} = 2$  and  $N_{EL} = 40$ : +42.5% for EBBM versus +46.6% for  $N = 4$ .

The fourth assessment completes the analysis of the structural method with a further tapered configuration, named  $D$ . By using the same aerodynamic parameters and boundary conditions as those involved for wing  $A$ , Table 8 summarizes the combined convergence of  $u_{z \max}$  on  $N$  and  $N_{EL}$ . The structural convergence as  $N$  increases is guaranteed and the conclusions about Poisson's locking correction formerly introduced are still valid. On the contrary, the difference between theories is less evident for configuration  $D$  than for configuration  $A$ . This applies mainly because the torsion of the tip cross-section is less significant for the unswept wing than the swept one. This makes the classical theories effective at least in the computation of the maximum displacement compared to  $N = 4$ , which offers the result closest to the Nastran solution.

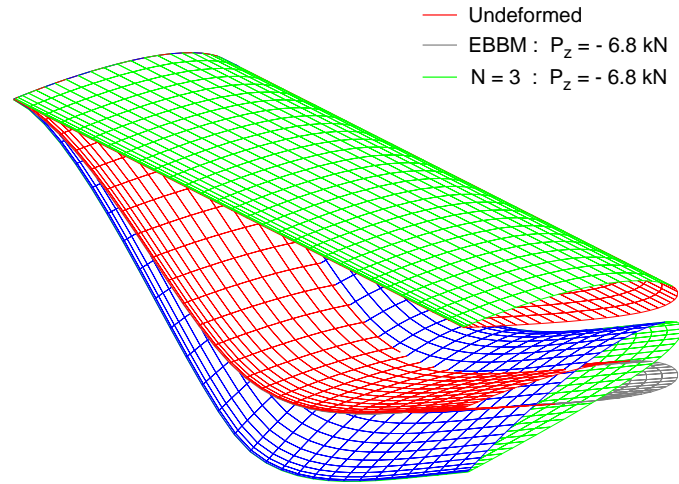
Fig. 8b shows trends which in some respects are similar to Fig. 8a. They share the deflection decrease as  $N_{EL}$  increases, so confirming that the taper ratio is the dominant parameter on the numerical convergence. As a consequence, a notable difference between  $N_{EL} = 2$  and  $N_{EL} = 40$  appears again: +42.6% for Euler-Bernoulli's theory and +36.3% for fourth-order model. However, the convergence on  $N_{EL}$  is achieved, so confirming the method's numerical consistency for dihedral wings as well as straight, swept, and tapered ones.

**Table 9:** Load cases applied to the wing configurations.

| Load Case ID      | 1    | 2    | 3        | 4    | 5       | 6       |
|-------------------|------|------|----------|------|---------|---------|
| Configuration     | B    | A    | A        | E    | E       | A, E, F |
| $V_\infty$ [m/s]  | 70   | 70   | 70       | 70   | 70      | 70      |
| $\alpha$ [deg]    | 5    | 5    | 5        | 5    | 5       | 5       |
| Force $P_z$ [kN]  | -6.8 | -7.2 | -20      | -7.2 | -20     | -       |
| Position $P_z^a$  | 50%  | 50%  | 30%      | 50%  | 30%     | -       |
| Twist $T_y$ [kNm] | -    | -    | -5, 0, 5 | -    | 0, 3, 6 | -       |
| Position $T_y^b$  | -    | -    | 30%      | -    | 30%     | -       |

<sup>a</sup> Position  $y_P$  along the spanwise direction:  $y_P/L$

<sup>b</sup> Position  $y_T$  along the spanwise direction:  $y_T/L$

**Figure 9:** Comparison of classical and higher-order models for configuration *B*. Load case 1.

### 7.3 Analysis of Significant Load Cases

Previous sections have clearly proved the effectiveness of both the structural and aerodynamic models. In this section, a combination of these two is applied to analyze significant *load cases*, which are listed in Table 9. They would simulate a number of flight conditions, by combining aerodynamic, bending and torsional loadings together.

Load case 1 is a transverse force  $P_z$  applied to the straight wing *B*, which is exposed to a free stream  $V_\infty = 70$  [m/s] with  $\alpha = 5^\circ$ . These values for the aerodynamic parameters will remain unchanged for load cases 1-6. The aerodynamic mesh has  $4 \times 40$  VLM panels whereas 20 *B4* elements discretize the structure.  $P_z$  is placed at 50 % of the span and equally split upon the two spars. It could simulate the effect of an inertial load along  $z$  axis due to wing engines, missiles, nacelles, or drop tanks.

The aerodynamic load generates a combination of bending and torsional stress.  $P_z$  has a non-negligible clockwise torsional effect since its application point does not coincide with the cross-section's center of twist. However, it provides an overall reduction of the transverse displacement, which reaches its maximum value at the leading edge of the tip cross-section. A comparison between Euler-Bernoulli's beam theory and the third-order model is shown in Fig. 9 (the tridimensional deflections are drawn by means of a large scale factor to clearly portray their differences). It is evident that the model  $N = 3$  has the capability to show the torsional effect, while EBBM turns out to be less effective in this combined load case.

Load case 2 combines a transverse force  $P_z$  and an aerodynamic load on the swept wing *A*. Because of the positive sweep angle, the whole structure would be expected to undergo a clockwise rotation about  $y$  axis due to the aerodynamics.

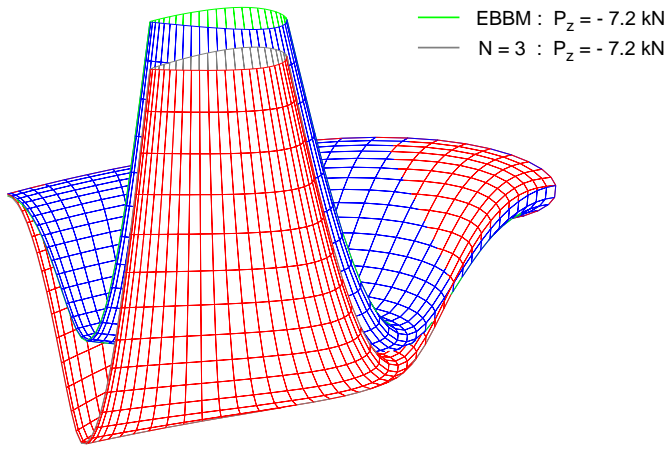


**Figure 10:** Tridimensional deformation of configuration A. Load case 2.

- N = 3 :  $P_z = -20 \text{ kN}$ ,  $T_y = -5 \text{ kNm}$
- N = 3 :  $P_z = -20 \text{ kN}$ ,  $T_y = 0 \text{ kNm}$
- N = 3 :  $P_z = -20 \text{ kN}$ ,  $T_y = +5 \text{ kNm}$
- EBBM :  $P_z = -20 \text{ kN}$ ,  $T_y = -5, 0, +5 \text{ kNm}$

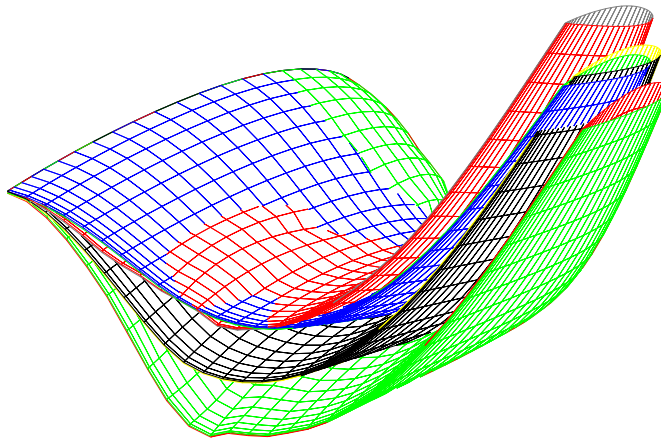


**Figure 11:** Effect of the variable torsional load on configuration A. Load case 3.

When  $P_z$  is also applied, it generates a counter-clockwise twist able to contrast the aerodynamic effect. When  $\Lambda$  is positive, the trailing edge is more sensitive to a bending load, even if the latter were placed at the airfoil's center of twist. In the case of a negative  $\Lambda$ , the same applies to the leading edge. The position of  $P_z$  behind the cross-section's center of twist gives an additional clockwise torsional effect, which is especially evident at 50 % of the span. In Fig. 10 the third-order model shows that this local twist impacts on the overall structure. The limits of EBBM are again evident, even for a bending case.

In load case 3, a torsional load  $T_y$  is added to load case 2.  $T_y$  could simulate inertial loads along  $x$  axis due to wing engines, missiles, and drop tanks located below the wing surface. The analysis of the swept wing A as the torsion  $T_y$  increases is made again with a third-order model and its results are in Fig. 11. The local deflection near the application points ( $y_P = y_T$ ) becomes more evident as  $T_y$  increases, whereas  $u_z$  decreases at the tip. In particular, the twist warps the trailing more than the leading edge of each cross-section. On the contrary, Euler-Bernoulli's theory is again unable to detect any twist. The figure underlines once more how  $N = 3$  model is capable to evaluate different flight conditions.

Further conclusions are obtained by considering the wing configuration named with letter E. As far as load case 4 is concerned, the transverse force  $P_z$  reduces the transverse displacement but introduces two opposite twist effects. The

**Figure 12:** Tridimensional deformation of configuration *E*. Load case 4.

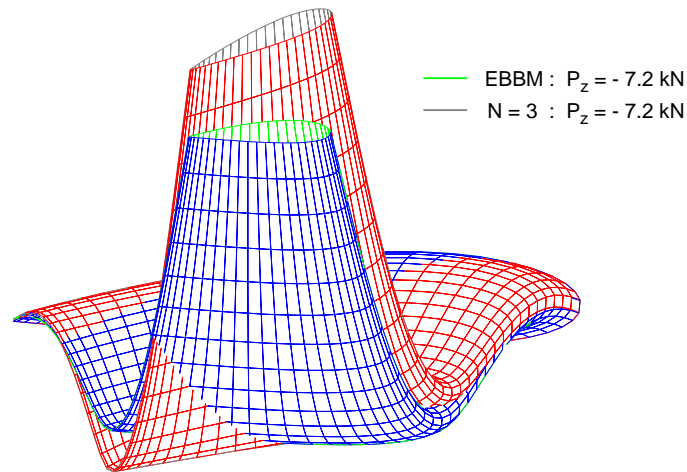
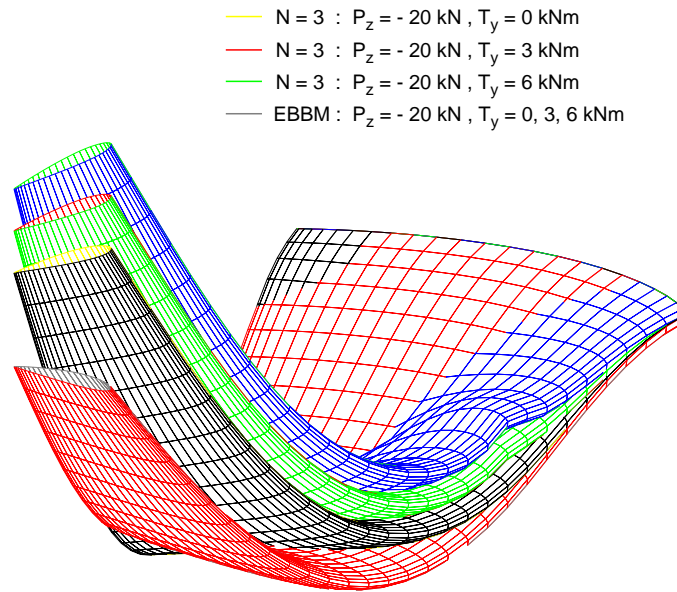


**Figure 13:** Effect of the variable torsional load on configuration *E*. Load case 5.



application point behind the cross-section's center of twist generates a counter-clockwise rotation, whereas an opposite torsion is due to the negative sweep angle. In conclusion, Fig. 12 displays the counter-clockwise twist of the overall wing obtained by means of a higher-order model. EBBM does not detect the proper deformation and  $u_{z \max}$  is underestimated.

Load case 5 involves  $P_z$  and torsion  $T_y$ , which are both placed at 30 % of the span of configuration *E*. Fig. 13 shows the increasing local effect on the most stressed cross-section. When the twist is higher, the transverse displacement at the tip increases for the forward swept wing. Such a behavior is opposite to the swept configuration *A*. In the same manner, a positive  $T_y$  does not countervail the typical torsion due to the aerodynamics when forward swept geometry is involved. For the generic cross-section, now the realistic center of rotation seems to be placed behind the center of twist. While for wing *A* the change of twist in value mainly rotates the trailing edge, only slightly involving the leading edge, wing *E* undergoes a notable variation in  $u_z$  on the leading edge, too. Such a point is presumably due to the negative sweep angle, which turns the leading edge to the "weak side". The discussion of results would not have been possible by relying on only classical beam models.

By considering the most constraining twist ( $T_y = 6$  kNm) of load case 5, the transverse shear stress  $\tau_{xz}$  along the charged cross-section is investigated

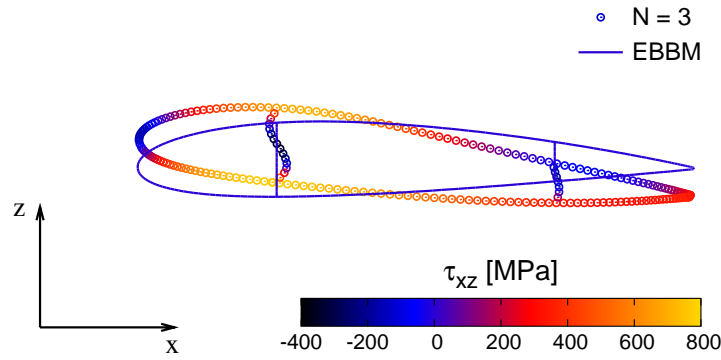


**Figure 14:** Distribution of the transverse shear stress  $\tau_{xz}$  on the deformed airfoil cross-section (30% span). Load case 5.

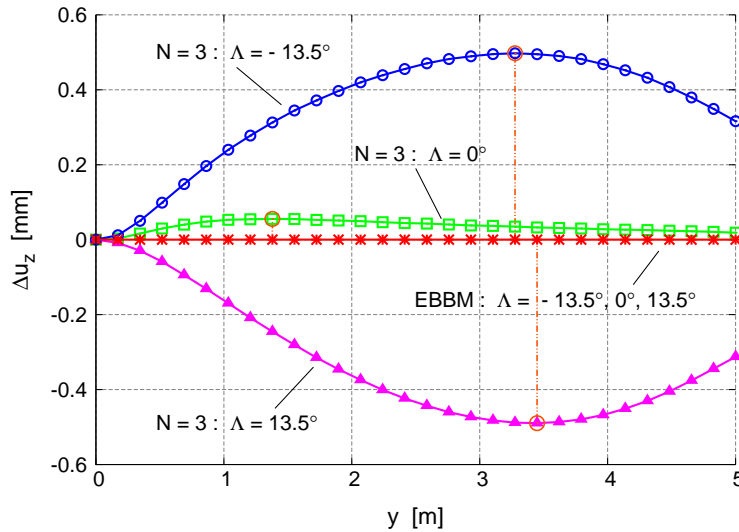


**Figure 15:** Effect of sweep angle on the torsional response of configurations A, E, and F subjected to aerodynamic pressure distribution. Load case 6.

with a third-order model. The distribution is presented in Fig. 14. Obviously, Euler-Bernoulli’s beam theory fails to detect any transverse shear effect. It is to be noticed that the linear and higher-order terms of  $u_x$  and  $u_z$  cannot be neglected. In fact, the shear effects are remarkable in such a constraining load case. In particular, the highest values of  $\tau_{xz}$  are placed at the joint points between the airfoil and the spar at 25% of the chord. Such a spar is highly stressed, reaching both the maximum and minimum values. On the contrary, the rear spar seems to not undergo high values of transverse shear stress. It is to be noticed the high rate of stress placed at the trailing edge and slightly below the leading edge. Fig. 14 illustrates how the proposed 1D model is able to portray the cross-section’s deformation. The spar straining is drawn with a large scale factor; however, it could be prevented by the introduction of transverse ribs [19], which here are not taken into account.

Load case 6 involves neither bending nor torsional loadings. The purpose is to analyze the effect of sweep angle on wings exposed to a free stream velocity  $V_\infty = 70$  [m/s] with  $\alpha = 5^\circ$ . The unswept configuration F is considered and compared to A and E, with  $\Lambda$  equal to  $13.5^\circ$  and  $-13.5^\circ$ , respectively. This choice is purpose-made, since the wings have all the same geometrical parameters with the exception of sweep angle. The analysis investigates the structural torsion along the spanwise direction due to the only aerodynamic pressure by means of the quantity  $\Delta u_z$ . It is defined as the difference of  $u_z$  between leading and trailing edges. The simulation is performed for each case via EBBM and third-order model and Fig. 15 shows the results.

At first glance, the twist is more significant when the sweep angle is high. Nevertheless, the unswept wing also undergoes a twist, since the aerodynamic load is a combination of bending and torsion. In particular, the rotation about

**Table 10:** Comparison of  $u_{z \max}$  [mm] for the structural and aeroelastic cases through different beam models. Flat plate.

| $V_\infty = 30 \text{ m/s}$ | $\alpha = 1 \text{ deg}$ | 10 × 50 panels |         | 20 B4 elements |         |
|-----------------------------|--------------------------|----------------|---------|----------------|---------|
|                             | EBBM                     | TBM            | $N = 3$ | $N = 4$        | Nastran |
| Structural analysis         | 68.650                   | 68.649         | 66.804  | 66.947         | -       |
| Aeroelastic analysis        | 68.611                   | 68.611         | 73.241  | 73.397         | 73.731  |
| % Difference                | -0.057                   | -0.055         | +9.636  | +9.635         | -       |
| DOFs                        | 305                      | 305            | 1830    | 2745           | 2135    |

$y$  axis is positive and its maximum is not placed at the tip cross-section. As expected and explained above, the rotation is positive for the forward swept wing  $E$  and negative for the swept  $A$ . It should be noted that the corresponding lines in Fig. 15 are not symmetrical with respect to the horizontal axis. Their maximum absolute values are not at the same  $y$  coordinate and this means that the shape of  $\Delta u_z$  depends on the sweep angle's sign, too.

As expected, Euler-Bernoulli's beam theory neglects any torsion and makes no difference among wings. Instead, Fig. 15 could be very helpful to the design and the evaluation of aeroelastic behavior of wings. Again, the capability of higher-order models applied to unidimensional finite elements via the CUF is proved.

#### 7.4 Preliminary Results on Static Aeroelastic Response

A preliminary aeroelastic case is now considered. The static aeroelastic response of a flat plate exposed to a free stream velocity  $V_\infty = 30$  [m/s] with  $\alpha = 1^\circ$  is investigated by solving the following aeroelastic system:

$$\mathbf{K}_{\text{aeroelastic}} \cdot \mathbf{q} = \mathbf{L}_{\text{RHS}} \quad (44)$$

For the sake of brevity, more details about the construction of  $\mathbf{K}_{\text{aeroelastic}}$  are not reported here but can be found in [18]. The flat plate has a thickness equal to 20 [mm], whereas its dimensions from a top view perspective are the same as those for configuration  $B$ . The structural analysis is also carried out by solving Eq. 42 for different beam models. As reported in Table 10, the increasing expansion order  $N$  enhances the gap between the structural and aeroelastic responses by approaching Nastran results (sol 144) through a limited number of degrees of freedom. Classical theories, EBBM and TBM, are unable to handle the proper torsional behavior and then are ineffective especially when the aeroelastic effect on the wing is relevant.

The effect of the free stream velocity on the maximum transverse displacement at the tip cross-section is evaluated in Fig. 16. The simulation is performed via a fourth-order approximation for both the structural and aeroelastic cases. The aeroelastic contribution to the system stiffness results to be more evident as  $V_\infty$  increases in good agreement with Nastran. A  $N = 4$  theory detects that the increasing free stream velocity enhances the aeroelastic coupling effect on the flat plate. For the sake of completeness, further static aeroelastic results on a number of metallic and composite made wing configurations are presented in [18].

## 8. Conclusions

This paper has proposed the coupling between the Vortex Lattice Method and a refined one-dimensional structural model with in-plane warping and plate/shell capabilities. The static response of wings with different geometries and cross-sections (mainly thin-walled airfoil) has been analyzed. The aerodynamic, structural, and coupling models have been assessed based on available results from

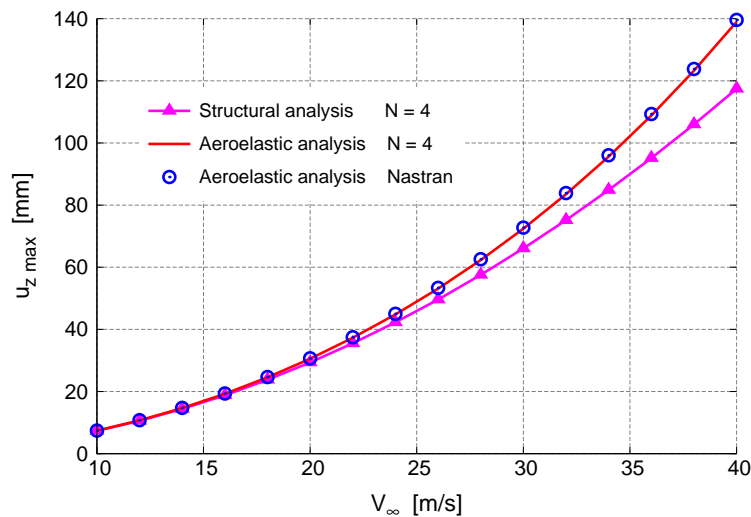


**Figure 16:** Effect of  $V_\infty$  on  $u_z$  max. Comparison of the structural and aeroelastic cases. Flat plate.

literature as well as on MSC Nastran code. The effectiveness of the coupling has been proved for various load cases as well as its advantages with respect to MSC Nastran model in terms of computational cost. Future work will address an aeroelastic static and dynamic analysis (divergence and flutter) and its application to wings made of composite material.

## References

- [1] S. Banerjee and M. Patil. Aeroelastic analysis of membrane wings. In *49th AIAA/ASME/ASCE/AHS/ASC Structures, Structural Dynamics, and Materials Conference*, AIAA Paper 2008-1812, Orlando, Florida, 7-10 April 2008.
- [2] K.J. Bathe. *Finite element procedure*. Prentice hall, Upper Saddle River, New Jersey, 1996.
- [3] V.L. Berdichevsky, E. Armanios, and A. Badir. Theory of anisotropic thin-walled closed-cross-section beams. *Composites Engineering*, 2(5-7):411–432, 1992.
- [4] R.L. Bisplinghoff, H. Ashley, and R.L. Halfman. *Aeroelasticity*. Addison-Wesley, Cambridge, 1995.
- [5] E. Carrera. A class of two dimensional theories for multilayered plates analysis. *Atti Accademia delle Scienze di Torino, Memorie Scienze Fisiche*, 19-20:49–87, 1995.
- [6] E. Carrera. Theories and finite elements for multilayered, anisotropic, composite plates and shells. *Archives of Computational Methods in Engineering*, 9(2):87–140, 2002.
- [7] E. Carrera. Theories and finite elements for multilayered plates and shells: a unified compact formulation with numerical assessment and benchmarking. *Archives of Computational Methods in Engineering*, 10(3):216–296, 2003.
- [8] E. Carrera and S. Brischetto. Analysis of thickness locking in classical, refined and mixed multilayered plate theories. *Composite Structures*, 82(4):549–562, 2008.
- [9] E. Carrera and S. Brischetto. Analysis of thickness locking in classical, refined and mixed theories for layered shells. *Composite Structures*, 85(1):83–90, 2008.

- [10] E. Carrera, S. Brischetto, and A. Robaldo. Variable kinematic model for the analysis of functionally graded material plates. *AIAA Journal*, 46:194–203, 2008.
- [11] E. Carrera and G. Giunta. Refined beam theories based on a unified formulation. *International Journal of Applied Mechanics*, 2(1):117–143, 2010.
- [12] E. Carrera, G. Giunta, P. Nali, and M. Petrolo. Refined beam elements with arbitrary cross-section geometries. *Computers and Structures*, 88(5–6):283–293, 2010.
- [13] E. Carrera and M. Petrolo. On the effectiveness of higher-order terms in refined beam theories. *Journal of Applied Mechanics*, 78(2):021013.1–021013.17, 2010.
- [14] E. Carrera and M. Petrolo. Analysis of slender, thin walled, composite made structures with refined 1d theories. In *52nd AIAA/ASME/ASCE/AHS/ASC Structures, Structural Dynamics, and Materials Conference*, AIAA Paper 2011-2168, Denver, CO, 4-7 April 2011.
- [15] E. Carrera, M. Petrolo, and P. Nali. Unified formulation applied to free vibrations finite element analysis of beams with arbitrary section. *Shock and Vibration*, 18(3):485–502, 2011.
- [16] E. Carrera, M. Petrolo, and A. Varello. Advanced beam formulations for free vibration analysis of conventional and joined wings. *Journal of Aerospace Engineering*, 2010. In press. DOI: 10.1061/(ASCE)AS.1943-5525.0000130.
- [17] E. Carrera, M. Petrolo, and E. Zappino. Performance of cuf approach to analyze the structural behavior of slender bodies. *Journal of Structural Engineering*, 2011. In press. DOI: 10.1061/(ASCE)ST.1943-541X.0000402.
- [18] E. Carrera, A. Varello, and L. Demasi. A refined structural model for static aeroelastic response and divergence of metallic and composite wings. 2011. Submitted.
- [19] E. Carrera, E. Zappino, and M. Petrolo. Analysis of thin-walled structures with longitudinal and transversal stiffeners. 2011. Submitted.
- [20] MacNeal-Schwendler corp. Interconnection of the structure with aerodynamics. *MSC.NASTRAN Theoretical Manual, Ver. 68*, 1994.
- [21] G.R. Cowper. The shear coefficient in Timoshenko’s beam theory. *Journal of Applied Mechanics*, 33(2):335–340, 1966.
- [22] L. Demasi.  $\infty^3$  hierarchy plate theories for thick and thin composite plates: the generalized unified formulation. *Composite Structures*, 84(3):256–270, 2008.
- [23] L. Demasi and E. Livne. Aeroelastic coupling of geometrically nonlinear structures and linear unsteady aerodynamics: two formulations. *Journal of Fluids and Structures*, 25:918–935, 2009.
- [24] L. Demasi and E. Livne. Dynamic aeroelasticity of structural nonlinear configurations using linear modally reduced aerodynamic generalized forces. *AIAA Journal*, 47(1):71–90, 2009.
- [25] P. Dinis, D. Camotim, and N. Silvestre. GBT formulation to analyse the buckling behaviour of thin-walled members with arbitrarily ”branched” open cross-sections. *Thin-Walled Structures*, 44(1):20–38, 2006.
- [26] E.H. Dowell and K.C. Hall. Modeling of fluid-structure interaction. *Annual Review of Fluid Mechanics*, 33:445–490, 2001.

- [27] R. El Fatmi. Non-uniform warping including the effects of torsion and shear forces. Part I: A general beam theory. *International Journal of Solids and Structures*, 44(18-19):5912–5929, 2007.
- [28] R. El Fatmi. Non-uniform warping including the effects of torsion and shear forces. Part II: Analytical and numerical applications. *International Journal of Solids and Structures*, 44(18-19):5930–5952, 2007.
- [29] L. Euler. *De curvis elasticis*. Bousquet, Lausanne and Geneva, 1744.
- [30] C. Farhat, P. Geuzaine, and G. Brown. Application of a three-field nonlinear fluid-structure formulation to the prediction of the aeroelastic parameters of an F-16 fighter. *Computers & Fluids*, 32(3):3–29, 2003.
- [31] Y.C. Fung. *An Introduction to the Theory of Aeroelasticity*. Dover Publications, 2008.
- [32] V. Giavotto, M. Borri, P. Mantegazza, G. L. Ghiringhelli, V. Caramaschi, G. C. Maffoli, and F. Mussi. Anisotropic beam theory and applications. *Computers and Structures*, 16:403–413, 1983.
- [33] G.P. Guruswamy. A review of numerical fluids/structures interface methods for computations using high-fidelity equations. *Computers & Structures*, 80(1):31–41, 2002.
- [34] R. Harder and R.N. Desmarais. Interpolation using surface splines. *Journal of Aircraft*, 9(2):189–192, 1972.
- [35] R. Harder, R. MacNeal, and W. Rodden. A design for the incorporation of aeroelastic capability into Nastran. *NASA report*, 1977. N71-33303.
- [36] M.J. de C. Henshaw et al. Non-linear aeroelastic prediction for aircraft applications. *Progress in Aerospace Sciences*, 43(4-6):65–137, 2007.
- [37] D.H. Hodges and G.A. Pierce. *Introduction to Structural Dynamics and Aeroelasticity*. Cambridge University Press, 2002.
- [38] R. Jones. *Mechanics of Composite Materials*. Taylor & Francis, Philadelphia, 2<sup>nd</sup> edition, 1999.
- [39] R. Kamakoti and W. Shyy. Fluid-structure interaction for aeroelastic applications. *Progress in Aerospace Sciences*, 40(8):535–558, 2004.
- [40] K. Kapania and S. Raciti. Recent advances in analysis of laminated beams and plates, part I: Shear effects and buckling. *AIAA Journal*, 27(7):923–935, 1989.
- [41] K. Kapania and S. Raciti. Recent advances in analysis of laminated beams and plates, part II: Vibrations and wave propagation. *AIAA Journal*, 27(7):935–946, 1989.
- [42] J. Katz and A. Plotkin. *Low-Speed Aerodynamics*. Cambridge University Press, 2001.
- [43] A.V. Krishna Murty. On the shear deformation theory for dynamic analysis of beams. *Journal of Sound and Vibration*, 101(1):1–12, 1985.
- [44] L. Librescu and O. Song. On the static aeroelastic tailoring of composite aircraft swept wings modelled as thin-walled beam structures. *Composites Engineering*, 2:497–512, 1992.
- [45] I. Mechab, A. Tounsi, M.A. Benatta, and E.A. Adda Bedia. Deformation of short composite beam using refined theories. *J. Math. Anal. Appl.*, 34(6):468–479, 2008.

- [46] V.V. Novozhilov. *Theory of elasticity*. Pergamon Press, Oxford, 1961.
- [47] B. Popescu and D.H. Hodges. On asymptotically correct Timoshenko-like anisotropic beam theory. *International Journal of Solids and Structures*, 37:535–558, 2000.
- [48] J.N. Reddy. *Mechanics of laminated composite plates and shells. Theory and Analysis*. CRC Press, 2<sup>nd</sup> edition, 2004.
- [49] W. Rodden, R. Harder, and D. Bellinger. Aeroelastic addition to Nastran. *NASA contractor report*, 1979. 3094.
- [50] R. Schardt. Eine erweiterung der technischen biegetheorie zur berechnung prismatischer faltwerke. *Der Stahlbau*, 35:161–171, 1966.
- [51] R. Schardt. Generalized beam theory-an adequate method for coupled stability problems. *Thin-Walled Structures*, 19:161–180, 1994.
- [52] W. Shyy, H. Aono, S.K. Chimakurthi, P. Trizila, C.-K. Kang, C.E.S Cesnik, and H. Liu. Recent progress in flapping wing aerodynamics and aeroelasticity. *Progress in Aerospace Sciences*, 46(7):284–327, 2010.
- [53] N. Silvestre. Second-order generalised beam theory for arbitrary orthotropic materials. *Thin-Walled Structures*, 40(9):791–820, 2002.
- [54] N. Silvestre and D. Camotim. First-order generalised beam theory for arbitrary orthotropic materials. *Thin-Walled Structures*, 40(9):791–820, 2002.
- [55] I.S. Sokolnikoff. *Mathematical Theory of Elasticity*. McGraw-Hill, 1956.
- [56] S.P. Timoshenko and J.N. Goodier. *Theory of elasticity*. McGraw-Hill, New York, 1970.
- [57] A. Varello, L. Demasi, E. Carrera, and G. Giunta. An improved beam formulation for aeroelastic applications. In *51st AIAA/ASME/ASCE/AHS/ASC Structures, Structural Dynamics, and Materials Conference*, AIAA Paper 2010-3032, Orlando, Florida, 12-15 April 2010.
- [58] V.V. Volovoi, D.H. Hodges, V.L. Berdichevsky, and V.G. Sutyrin. Asymptotic theory for static behavior of elastic anisotropic I-beams. *International Journal of Solid Structures*, 36(7):1017–1043, 1999.
- [59] K. Washizu. *Variational methods in elasticity and plasticity*. Pergamon Press, Oxford, 1968.
- [60] J.R. Wright and J.E. Cooper. *Introduction to Aircraft Aeroelasticity and Loads*. John Wiley & Sons, 2008.
- [61] W. Yu and D.H. Hodges. Generalized Timoshenko theory of the variational asymptotic beam sectional analysis. *Journal of the American Helicopter Society*, 50(1):46–55, 2005.
- [62] W. Yu, V.V. Volovoi, D.H. Hodges, and X. Hong. Validation of the variational asymptotic beam sectional analysis (VABS). *AIAA Journal*, 40(10):2105–2113, 2002.
- [63] Inc. ZONA Technology. Spline methods for spline matrix generation. *ZAERO Theoretical Manual, Ver. 7.1*, 2004.